RESEARCH

# Data-Driven Brain Tumor Classification Using CNNs with Trainable Gabor and LoG Feature Mining Layers

**Ghada Atteia · Nabeel Ahmed Khan · Raed Alharthi · Abeer Aljohani · Shtwai Alsubai · Muhammad Umer · Xiaochun Cheng**

Received: 26 October 2025 / Revised: 25 February 2026 / Accepted: 18 March 2026


**Abstract**
Magnetic resonance imaging (MRI) is an important method for reproducible brain tumour diagnosis. Conventional convolutional neural networks (CNNs) and transfer learning models have been demonstrated to yield high accuracy, but are not yet without certain shortcomings in terms of domain shifts, interpretability, and suboptimal feature generalization at a lower level. This work introduces a novel hybrid architecture using trainable CNN coupled with Gabor and Laplacian of Gaussian (LoG) modules to sequentially learn textural and edge-based features. The model is evaluated against an open-source Brain Tumor MRI dataset with conditions including glioma, meningioma, pituitary and no-tumor. The proposed model achieves an overall accuracy of 96%, with better accuracy compared to baseline CNN performance and high interpretability in terms of learned kernels and saliency maps which provide clinically interpretably outputs.

**Keywords** Brain tumor classification · MRI imaging · Convolutional neural networks · Enhanced gabor filters · Laplacian of gaussian · Deep learning · Medical image analysis · Interpretability · Grad-CAM · Feature extraction

## 1 Introduction

The accurate classification of brain tumors is one of the most important research issues in the area of medical imaging, due to the necessity of early diagnosis and precise treatment planning based on Magnetic Resonance Imaging (MRI). A revolutionary change has been observed in this field with the advent of the deep learning, specifically convolutional neural networks (CNNs). The initial work was based on training CNNs from scratch on small datasets. For example, in [1] 98.7% accuracy was obtained by using the custom CNN model, whereas in [2] 99% accuracy on training set and 96% accuracy on test set were reported. The capabilities of the CNN's to autonomously learn the features in a hierarchial way are clearly evident by the results from existing works, however the limitations of these networks are also exposed in terms of overfitting, poor generalization across the heterogeneous clinical data, and sensitivity to variations in imaging protocols.

To address such problems, researchers resorted to transfer learning using pre-trained models. For example, in [3], VGG16 (94.8%) was used with a rich feature representation trained on a large natural image dataset, and



Published online: 04 April 2026

in [4] VGG19 (95.4%) and in [5] AlexNet (97.5%) were used. Even though the performance was improved, the domain mismatch between medical and natural images made it challenging to capture modality-specific patterns (i.e., textural heterogeneity, subtle intensity gradients) that are needed for a successful tumor classification [6].

New trends emerge over the years such as the rise of residual architectures to combat vanishing gradients in CNNs [7] and hybrid architectures such as CNN-SVM are successfully used for fine-tuning the decision boundaries [8]. While aggressive data augmentation and light weight design have been adopted due to the need for clinical applicability of these networks [9, 10], Capsule Networks [11] and multistage pipelines [12] have focused on maintaining the space hierarchies as well as multi-objective tasks of fusion of segmentation and classification towards accurate diagnosis. In the recent works, Vision Transformers (ViTs) and Hybrid CNN-ViT models proved to be efficient in the context of handling of multi-modality inputs and long-range dependencies [13–16]. However, these methods tend to be computationally expensive and low-level MRI-specific features such as edges and textures are not given explicit priors.

Over the years, the integration of Gabor filters into convolutional networks has significantly matured [17, 18]. Initial work demonstrated that the modulation of standard convolution with orientation-tuned Gabor kernels created an inherent ease of adaptability to changes in scale/rotation, allowing the model to capture textured images more reliably. Subsequently, architectures were created, in which the first few layers were forced to obey the Gabor model - parameters of spread, wavelength, phase arbitrary during training. This approach enhanced training speed and clarity of features. In addition, the filters remained wave-like and interpretable [19, 20]. Other work has focused on Gabor constraints in lower-level architectures ResNets. Here, Gabor filters enhanced adversarial robustness without sacrificing accuracy. Other parallel work used Gabor filters to adjust/optimize parameters and speed training in low-resource settings. Our work carries this lineage into the most difficult area of brain tumour MRI scans, and by confining Gabor parameters within some reasonably biologically plausible bounds, and using them in conjunction with a Laplacian-of-Gaussian edge detector, we create a front-end that, in a sense, translates to cortical receptive fields and remains sensitive to the fine textures and edges that differentiate gliomas, meningiomas, and pituitary tumors, and this provides performance, but also clinically relevant and reliable feature maps.

However, some challenges remain: the non-diverse range of datasets, non-interpretable outcomes, high inference costs, and inconsistent performance across institutions and MR sequences (i.e. T1, T2, FLAIR). Most methods are based on 2D slices, sufferers from modality bias, and do not provide insight into model decisions - three key flaws that make them difficult for clinical adoption. These challenges can be summed up as:

1. Limited interpretability and generalization in conventional CNNs for medical imaging.
2. Insufficient clinical trustworthiness of high-performing models.
3. Absence of domain-tailored, biologically grounded preprocessing in brain tumor classification.

To solve these issues, trainable Enhanced Gabor and Laplacian of Gaussian (LoG) filters in CNN architecture were used. These layers are biologically inspired and they work by learning tumor specific texture and edges patterns in an adaptive way, this mechanism help reduce the CNN burden of extracting the low-level features, and enhances its ability to handle different modality variations, this methodology also enables the clinical interpretability by using Grad-CAM visualizations, and learned filters responses. We hypothesize that this end-to-end unified trainable framework would be superior in terms of accuracy, generalization and diagnostic trustworthiness when compared to standard CNNs and transfer learned models.

In this study, a new framework based on the combination of improved Gabor layers and LoG layers with the CNN has been proposed for the robust, interpretable, and efficient brain tumor classification. This model pretrained on MRI-specific features and conditioned on MRI-specific patterns improves feature extraction, provides more insight into the feature importance through Grad-CAM and feature map analysis, and is computationally efficient for clinical application. The contribution of this paper lies in the following:

- Developed a new integrated framework of powerful Gabor and LoG layers with CNNs for robust brain tumor classification.

- Trainable and biologically constrained Gabor and LoG filters constrained applied in the CNN network were introduced to extract tumor-specific features with their texture and edge information crafted in an adaptive manner to solve issues of interpretability and generalization. Grad-CAM and feature maps enabled a more clinically understandable model and lowered the clinically adoption barrier through better model visualization.
- By using ablation studies we showed that our dual-feature extraction approach significantly improves the accuracy over baseline CNNs, providing the evidence of its effectiveness.

## 2 Methodology

Magnetic Resonance Imaging (MRI) data classification of brain tumors is highly problematic because of the variability of tumor morphology, minor differences in intensity, and textural characteristics among different modalities, including T1, T2 and FLAIR. To overcome these, this paper presents a coherent model as shown in Figure 1 combining both improvements in Gabor filter layers and Laplacian of Gaussian (ogan) layers with a

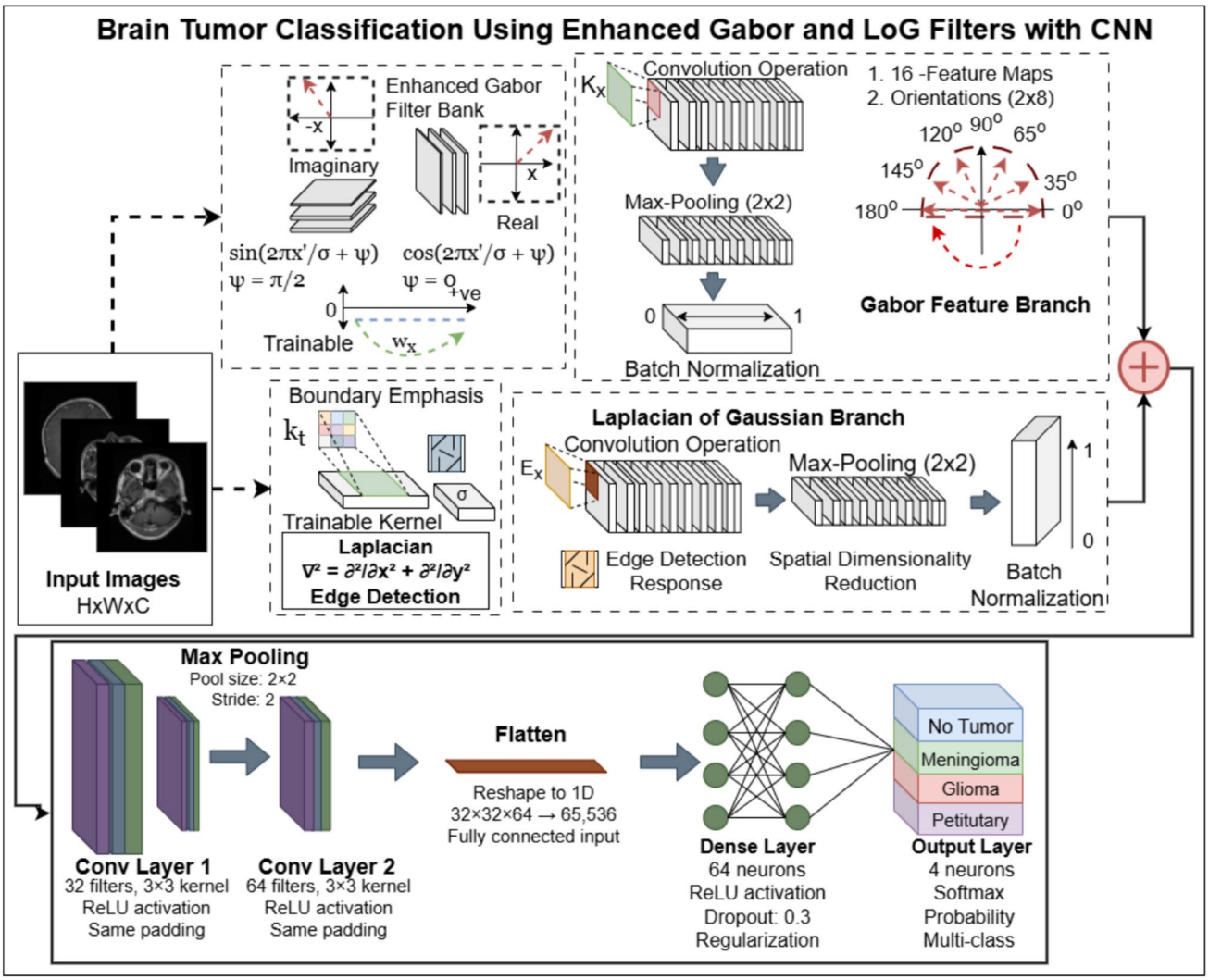


**Fig. 1** Visual illustration of proposed framework for classifying brain tumors using MRI images with integrated Enhanced Gabor Filter Layer, LoG (Laplacian of Gaussian) Layer, and Convolutional Neural Networks (CNN) modules for end-to-end trainable architecture

convolutional neural network (CNN) to realize effective and explainable tumor classification. The texture analysis is biologically driven and the edges are enhanced to extract domain specific features, which are orientated through a CNN to provide multi-class classification (e.g., meningioma, glioma, pituitary tumor, healthy). In this section, the general implementation plan, the relevance of CNNs to it, the drawbacks of baseline Gabor filters and their suggested improvements, the detection capabilities of the LoG layer, and the unified approach with mathematical justifications are described. The strategy is centered on the theoretical rigor, which aims at the improvement of feature extraction of brain tumor classification, and overcomes challenges such as variability of data sets and clinical usability.

### 2.1 Overall Implementation Strategy

A hybrid model that integrates domain specific feature extraction and deep learning for final classification is proposed for an optimal workflow in brain tumor classification. The proposed model consists of parallel branches, one of which consists of enhanced Gabor filter layers that capture textures in multiple scales and the other consists of Log layers that capture edge, which are important when it comes to delineating tumor boundaries. Each of the branches generates feature maps that are then concatenated to be input into a CNN that learns hierarchical representation for the classification task. The entire frame is end to end trainable which means Gabor and Log layers can learn their parameters in conjunction with the CNN, thus ensuring the pipeline is synchronized with the intricacies of the MRI data. This single model addresses many of the individual CNNs in medical imaging, like data hunger and the lack of interpretability [21].

Mathematically, the framework can be expressed as a composite function:

$$f(X) = \mathrm{CNN}(\mathrm{Concat}(\mathrm{Gabor}(X), \mathrm{LoG}(X))),$$

where $X \in \mathbb{R}^{H\times W\times C}$ is the input MRI image with height $H$, width $W$, and channels $C$, $\mathrm{Gabor}(X)$ and $\mathrm{LoG}(X)$ denote the feature maps from the respective layers, and $\mathrm{CNN}(\cdot)$ represents the convolutional backbone. The concatenated feature maps form a tensor $F \in \mathbb{R}^{H\times W\times K}$, where $K$ is the combined number of feature channels. This structure enhances feature extraction by integrating texture and edge information, critical for distinguishing tumor types in MRI data [22]. The trainable preprocessing layers reduce the CNN's burden of learning low-level features, improving robustness and interpretability for clinical applications.

### 2.2 Convolutional Neural Networks in Brain Tumor Classification

CNNs are being used for medical image analysis because of their ability to analyze and respond to complex hierarchies from raw data [23]. For brain tumor classification, CNNs can recognize even the slightest differences in the spatial characteristics, tumor shapes, and textures amongst various classes of tumors. For this CNN architecture, we have aimed to achieve optimal efficiency and performance by fusing and filtering the Gabor and LoG feature maps to create high-order representations for the classification of multiple classes. This CNN uses convolutional layers with ReLU and max pooling for intermediate spatial reductions, and during the dense layers, dropout is used to limit the effect of overfitting. For decision-making and classification, the last layer uses softmax.

The convolutional operation is defined as:

$$(F * k)(x, y) = \sum_{m,n} F(x + m, y + n)k(m, n),$$

where $F$ is the input feature map, $k \in \mathbb{R}^{k_h\times k_w}$ is the kernel, and $(x, y)$ are spatial coordinates. The ReLU activation, $\mathrm{ReLU}(z) = \max(0, z)$, introduces non-linearity, enabling the model to capture complex patterns like irregular tumor boundaries. Max-pooling reduces spatial dimensions:

$$\mathrm{Pool}(F)_{i,j} = \max_{m,n\in\mathrm{window}} F(i + m, j + n),$$

improvement of the translational invariance and computational efficiency, which is important for accommodating the variations in the tumor location [24]. Another advantage of the CNN is that it is efficient, as it uses preprocessed Gabor and LoG features, so deep architectures that are highly susceptible to overfitting on small medical data sets, are not necessary [25]. This renders the CNN especially useful in the task of brain tumor classification, where it is important to use features synthesized with high accuracy to discriminate between tumor types that exhibit some overlapping characteristics. Only two convolutional block are used in the shallow architecture design (because the feature maps are rich enough in the Gabor+LoG layers).

### 2.3 Enhanced Gabor Filter Layers

Gabor filters, inspired by the human visual system's response to spatial frequencies and orientations, are well-suited for analyzing the complex textural patterns in MRI images [26] as depicted in Fig. 2. However, baseline Gabor filters, defined as:

$$g(x, y; \sigma, \theta, \lambda, \psi) = \exp\left(-\frac{x'^2 + y'^2}{2\sigma^2}\right) \cdot \cos\left(2\pi\frac{x'}{\lambda} + \psi\right),$$

where $x' = x\cos\theta + y\sin\theta$, $y' = -x\sin\theta + y\cos\theta$, $\sigma$ is the Gaussian spread, $\theta$ is the orientation, $\lambda$ is the wavelength, and $\psi$ is the phase offset, have limitations.

These include fixed parameters that fail to adapt to the diverse scales and textures of brain tumors, leading to suboptimal feature extraction for heterogeneous tumors like gliomas [27]. Additionally, static filters struggle to generalize across MRI modalities with varying contrast and noise profiles.

To overcome these, the proposed enhanced Gabor filter layers introduce multi-scale ($\sigma$) and multi-orientation ($\theta$) configurations, with trainable kernels and parametric configuration given in Table 1. The real and imaginary components are:

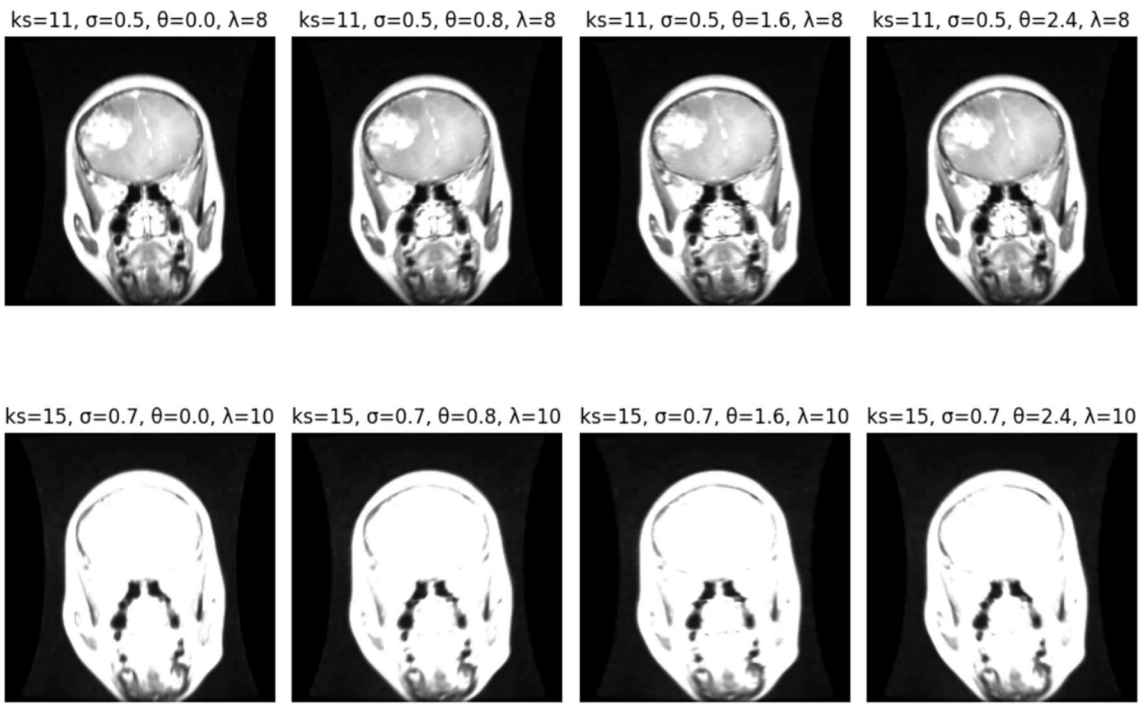


**Fig. 2** Gabor filter-based representation of an input MRI image, highlighting the textural features extracted through multi-scale and multi-orientation kernels, demonstrating the Enhanced Gabor Layer's role in capturing tumor-specific patterns

**Table 1** Parameters of the enhanced gabor filter layer

| Parameter | Value/Range |
|---|---|
| Number of Orientations $\theta$ | 8 (uniformly sampled from 0 to $\pi$) |
| Kernel Size | $7 \times 7$ |
| Scales ($\sigma$) | Trainable via softplus-transformed log-$\sigma$, initialized to yield $\sigma \approx 1.5$–3.0 |
| Wavelength ($\lambda$) | Trainable via softplus-transformed log-$\lambda$, constrained to maintain $\lambda/\sigma \approx 0.5$–1.5 |
| Phase $\psi$ | Trainable, uniformly sampled from 0 to $2\pi$ |
| Aspect Ratio $\gamma$ | Trainable via scaled sigmoid, constrained to [0.2, 0.9] |
| Trainable | Yes, with parametric constraints |

$$g_{\text{real}}(x, y; \sigma, \theta) = \exp\left(-\frac{x'^2 + y'^2}{2\sigma^2}\right) \cdot \cos\left(2\pi \frac{x'}{\sigma}\right),$$

$$g_{\text{imag}}(x, y; \sigma, \theta) = \exp\left(-\frac{x'^2 + y'^2}{2\sigma^2}\right) \cdot \sin\left(2\pi \frac{x'}{\sigma}\right).$$

For an input image $X \in \mathbb{R}^{H \times W \times C}$, the feature map is computed as:

$$F_{\text{Gabor}}(x, y, k) = \sum_{c=1}^{C} (X_c * g_{\sigma,\theta,\psi})(x, y),$$

where $k$ indexes the filter (combinations of $\sigma$, $\theta$, and $\psi \in \{0, \pi/2\}$ for real and imaginary parts), and $*$ denotes convolution. The kernels are trained as parametrically constrained convolutional filters that are initialized by the traditional Gabor formula as in $k_{i,j} = g(x_i, y_j, ; sigma, theta, andpsigamma)$, with parameters ($\sigma$, $\theta$, $\lambda$, $\psi$, $\gamma$) learned in closed form under biological constraints $\theta$ uniformly over [0, $\pi$) reflecting V1 orientation selectivity [28], log-$\sigma$ and log-$\lambda$ via softplus yielding $\sigma \approx 1.5$–3.0 and maintaining $\lambda/\sigma \approx 0.5$–1.5 based on spatial frequency tuning in primate V1 [29], $\psi$ over [0, $2\pi$) for phase preferences [30], and $\gamma$ sigmoid-constrained to [0.2, 0.9] matching V1 aspect ratios [31]. The back-propagation involves back-propagating the gradients through the convolution operation to adjust the constrained parameters of the kernel that otherwise are fixed analytically. The parameters are explicitly learned during back-propagation while remaining within biologically plausible ranges, ensuring interpretability and preventing drift into generic filters, as Gabor functions best approximate V1 receptive fields [32]. We represent 8 independent $7 \times 7$ Gabor kernels (8 orientations, with trainable scale, wavelength, phase, and aspect ratio per orientation) and 1 $7 \times 7$ LoG kernel (see Table 1). Each of them is optimized together with the downstream CNN based on the same Adam optimization.

The computation of the Gabor feature map to an input image, X, is done through convolution:

$$F_{\text{Gabor}}(x, y, k) = \sum_{c=1}^{C} (X_c * k_{\sigma,\theta,\psi})(x, y),$$

where the kernel gradient is:

$$\nabla_k \mathcal{L} = \frac{\partial \mathcal{L}}{\partial F_{\text{Gabor}}} * X_c^{\top}.$$

The frequency response of a Gabor filter in the Fourier domain is:

$$G(u, v; \sigma, \theta) \propto \exp\left(-2\pi^2\sigma^2 \left[(u\cos\theta + v\sin\theta)^2 + (-u\sin\theta + v\cos\theta)^2\right]\right),$$

where $(u, v)$ are frequency coordinates. Such band-pass property allows the model to extract selective texture that improves tumors microcalcifications or irregular patterns detection by the model, which is even better than conventional mammography in detection and differentiation of tumor types [26]. Sensitivity to fine and coarse

textures is guaranteed by the multi-scale, whereas multiple orientations $\sigma \in \{1.5, 3.0\}$ are used by the method to address directional variations, enhancing the ability to discriminate between different types of tumor. The trainability relaxes the inflexibility of the baseline Gabor filters to allow the model to adapt to the ideal filter parameters of MRI-specific features, thereby improving the generalization challenges of previous studies, which have experienced them [6].

### 2.4 Laplacian of Gaussian (LoG) layers

LoG filters combine Gaussian smoothing with the Laplacian operator to detect edges, which are critical for delineating tumor boundaries in MRI images [33]. The baseline LoG filter is:

$$\mathrm{LoG}(x, y; \sigma) = -\frac{1}{\sigma^4}\left(x^2 + y^2 - 2\sigma^2\right) \exp\left(-\frac{x^2 + y^2}{2\sigma^2}\right).$$

For an input $X$, the feature map is:

$$F_{\mathrm{LoG}}(x, y) = (X * \mathrm{LoG}_\sigma)(x, y).$$

The Gaussian component suppresses noise, while the Laplacian, $\nabla^2 = \frac{\partial^2}{\partial x^2} + \frac{\partial^2}{\partial y^2}$, amplifies intensity changes. However, fixed $\sigma$ values in baseline LoG filters limit their adaptability to the varied edge profiles of brain tumors, such as the irregular boundaries of gliomas or the sharp transitions of meningiomas [22] depictied in Figure 3. The proposed enhancement introduces a parametrically constrained trainable LoG layer that preserves the exact

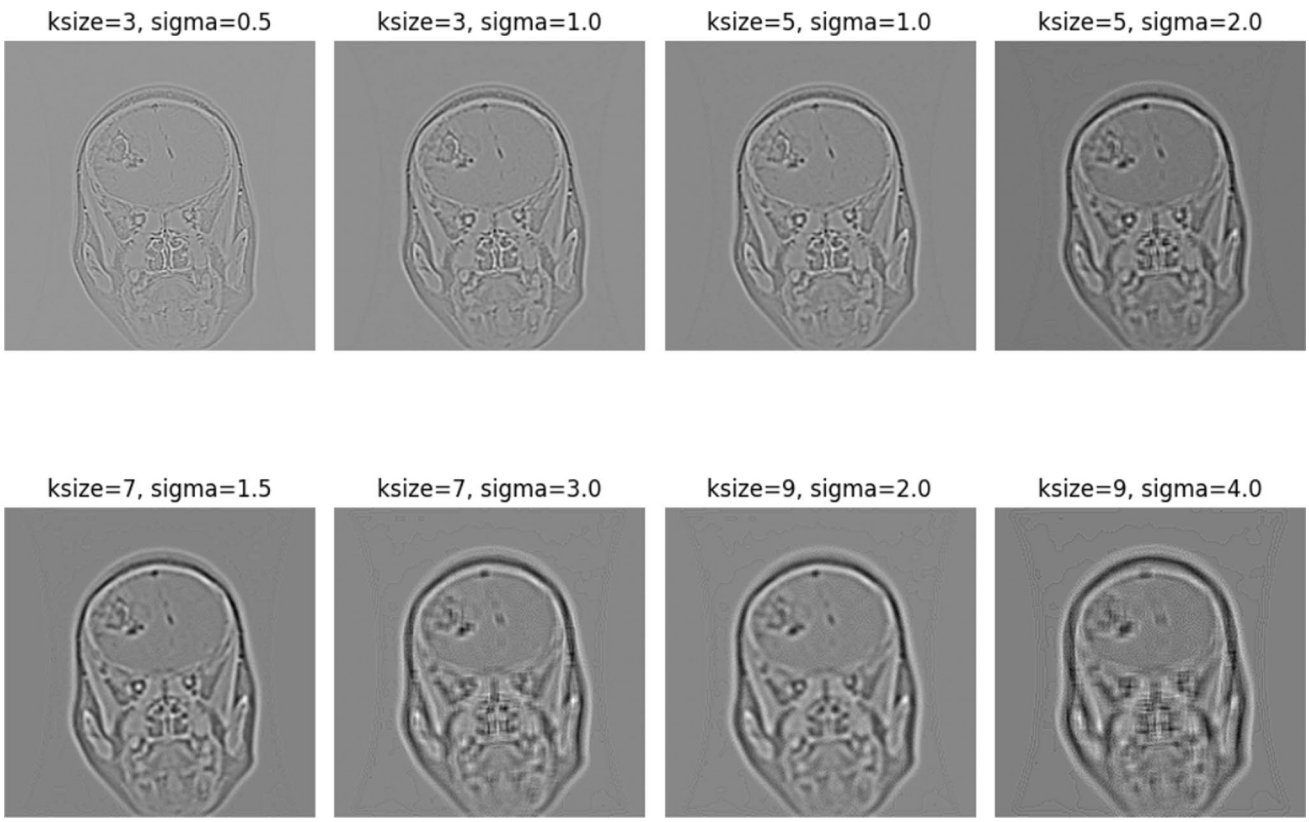


**Fig. 3** LoG filter-based representation of an input MRI image, emphasizing edge and boundary features extracted by the Laplacian of Gaussian Layer, illustrating its contribution to tumor delineation

**Table 2** Parameters of the Laplacian of Gaussian (LoG) layer

| Parameter | Value/Range |
|---|---|
| Kernel Size | $7 \times 7$ |
| Scale ($\sigma$) | Trainable, constrained to [0.5, 3.0], initialized at 1.5 |
| Trainable | Yes, with closed-form parametric constraint |
| Normalization | Zero-mean and amplitude-normalized |

mathematical LoG structure while allowing the scale parameter $\sigma$ to be learned in closed form. This ensures high interpretability and prevents drift into arbitrary filters, as the kernel is always generated analytically from the current $\sigma$. The learnable $\sigma$ is initialized at 1.5 and constrained to the biologically plausible range [0.5, 3.0] via clipping, reflecting typical center-surround receptive field sizes in retinal ganglion and LGN cells [33] and aligning with scale-space principles for edge detection [34], while the parameters of the LoG layer are given in Table 2.

The LoG's frequency response is derived from the Fourier transform of the Gaussian and Laplacian:

$$\mathcal{F}\{\mathrm{LoG}(x, y; \sigma)\}(u, v) \propto -(u^2 + v^2) \exp\left(-2\pi^2\sigma^2(u^2 + v^2)\right).$$

This high-pass behavior emphasizes edges, enhancing the model's ability to localize tumors. The trainable kernel, $k_{\mathrm{LoG}} \in \mathbb{R}^{k_h \times k_w \times C \times 1}$, adapts to specific edge scales, improving sensitivity to subtle transitions in MRI data. The edge-enhanced feature maps complement the texture-focused Gabor outputs, providing a robust representation for classification [35].

## 2.5 Consolidated Methodology and Enhancements

The consolidated methodology integrates enhanced Gabor and LoG layers with the CNN in a unified, end-to-end trainable framework. The process begins with parallel feature extraction:

$$F_{\mathrm{combined}} = \mathrm{Concat}(F_{\mathrm{Gabor}}, F_{\mathrm{LoG}}),$$

where $F_{\mathrm{Gabor}} \in \mathbb{R}^{H \times W \times K_1}$ and $F_{\mathrm{LoG}} \in \mathbb{R}^{H \times W \times K_2}$ are concatenated to form $F_{\mathrm{combined}} \in \mathbb{R}^{H \times W \times (K_1 + K_2)}$. The CNN processes this to produce class probabilities via a softmax function:

$$\hat{y} = \mathrm{softmax}(\mathrm{CNN}(F_{\mathrm{combined}})).$$

The loss function, sparse categorical cross-entropy, is:

$$\mathcal{L} = -\sum_{i=1}^{N} y_i \log(\hat{y}_i),$$

optimized via gradient descent to update all parameters, including Gabor and LoG kernels. The enhanced Gabor filters address baseline limitations by allowing multi-scale and multi-orientation adaptation, modeled as:

$$k_{\sigma,\theta,\psi} = \arg\min_{k} \mathcal{L}(X, y; k, \theta_{\mathrm{CNN}}),$$

where $\theta_{\mathrm{CNN}}$ are CNN parameters. This ensures filters align with tumor-specific textures. Similarly, the LoG kernel is optimized:

$$k_{\mathrm{LoG}} = \arg\min_{k} \mathcal{L}(X, y; k, \theta_{\mathrm{CNN}}),$$

adapting to edge profiles. The combined feature extraction enhances the CNN's input, reducing its learning burden and improving generalization [9]. The extracted features from the trainable Enhance Gabor and LoG Layers are illustrated in Fig. 4 The methodology's significance lies in its interpretable, domain-specific features, which address the challenges of tumor heterogeneity and clinical deployment constraints, paving the way for robust

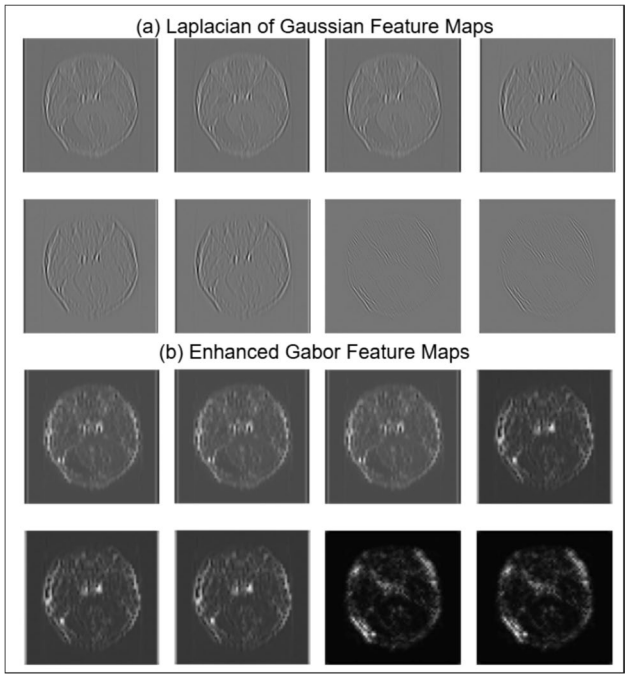


**Fig. 4** Feature maps generated from trainable parameterized LoG and Enhanced Gabor layers within the CNN network, showcasing the hierarchical feature extraction process for brain tumor classification, with distinct textural and edge representations

**Table 3** Parameters of the Convolutional Neural Network (CNN)

| Layer | Parameters |
|---|---|
| Input Layer | Shape: 128 × 128 × 3 |
| Gabor Branch Max-Pooling | Pool Size: 2 × 2 |
| Gabor Branch Batch Normalization | Applied |
| LoG Branch Max-Pooling | Pool Size: 2 × 2 |
| LoG Branch Batch Normalization | Applied |
| Convolutional Layer 1 | Filters: 32, Kernel Size: 3 × 3, Activation: ReLU, Padding: Same |
| Max-Pooling 1 | Pool Size: 2 × 2 |
| Convolutional Layer 2 | Filters: 64, Kernel Size: 3 × 3, Activation: ReLU, Padding: Same |
| Flatten | Applied |
| Dense Layer 1 | Units: 128, Activation: ReLU |
| Dropout | Rate: 0.3 |
| Output Layer | Units: 4, Activation: Softmax |

**Table 4** Hyperparameters for model training

| Hyperparameter | Value |
|---|---|
| Optimizer | Adam |
| Initial Learning Rate | $1 \times 10^{-3}$ |
| Loss Function | Sparse Categorical Crossentropy |
| Metric | Accuracy |
| Epochs | 30 |
| Learning Rate Scheduler | ReduceLROnPlateau (patience=5, factor=0.5) |
| Callbacks | ParameterLogger |

brain tumor classification. The overall parametric configuration and the hyperparameters selected for the model training are also given in Tables 3 and 4. The pseudo-algorithm of the proposed methodology is given as Algorithm 1.

### 2.6 Experimental Setup

All experiments were performed on Google Colab having an intel Xeon Processor at 2.3GHz with RAM 12GB. The GPU used was Tesla T4 with 16GB of graphic memory while the framework used for the training is Tensorflow 2.20. The data-split for training was kept at a usual 70:30 ratio. With 70% data used for training while 50% of the 30% test data was used for validation purpose and the remaining was used as held-out test set. For the pre-processing, a standard normalization is performed keeping the maximum at 1.0 and minimum pixel value at 0 considering a zero-mean unit-variance normalization per channel. The augmentation was performed at training time using the random horizontal/vertical, flip(0.5) and rotation based transformations.

**Require:** MRI image $X \in \mathbb{R}^{H \times W \times C}$
**Ensure:** Class probabilities $\hat{y} \in \mathbb{R}^N$
Initialize trainable parameters: Gabor kernels ($k_{\sigma,\theta,\psi}$), LoG kernel ($k_{\text{LoG}}$), CNN weights ($\theta_{\text{CNN}}$)
**Gabor Feature Extraction:**
**for** each $\sigma$, $\theta$, $\psi \in \{0, \pi/2\}$ **do**
    Compute Gabor kernel: $g(x, y) = \exp\left(-\frac{x'^2+y'^2}{2\sigma^2}\right) \cos\left(2\pi\frac{x'}{\sigma} + \psi\right)$
    Convolve: $F_{\text{Gabor}} = \text{Concat}([X_c * g]_{c=1}^{C})$
**end for**
Apply max-pooling and batch normalization: $F_{\text{Gabor}} = \text{BatchNorm}(\text{MaxPool}(F_{\text{Gabor}}))$
**LoG Feature Extraction:**
Compute LoG kernel: $\text{LoG}(x, y) = -\frac{1}{\sigma^4}(x^2 + y^2 - 2\sigma^2) \exp\left(-\frac{x^2+y^2}{2\sigma^2}\right)$
Convolve: $F_{\text{LoG}} = X * \text{LoG}$
Apply max-pooling and batch normalization: $F_{\text{LoG}} = \text{BatchNorm}(\text{MaxPool}(F_{\text{LoG}}))$
**Feature Concatenation:**
$F = \text{Concat}(F_{\text{Gabor}}, F_{\text{LoG}})$
**CNN Classification:**
Apply convolutional layers with ReLU: $F_{\text{conv}} = \text{ReLU}(F * k_{\text{CNN}})$
Apply max-pooling, flatten, dense layers with ReLU, and dropout
Compute: $\hat{y} = \text{softmax}(W \cdot F_{\text{dense}} + b)$
**Train:** Optimize $\mathcal{L} = -\sum_{i=1}^{N} y_i \log(\hat{y}_i)$ via gradient descent
**Return** $\hat{y}$

**Algorithm 1** Brain Tumor Classification with Enhanced Gabor and LoG

## 3 Results and Discussion

This section presents the findings from the study and the corresponding interpretation. To classify the brain tumors MRI brain images are used, and the heterogeneity of tumors is attempted to be tackled considering the problem of multi-class classification. In this section the results of the experiment are discussed, and the explainable aspects of the learned filter Gabor and LoG filter kernels are analyzed to explain the rationale behind the model. The components of the model are defended by the results of an ablation study. The study limitations are discussed and the future work is proposed.

### 3.1 Dataset Description

The data set used in this research to classify brain tumors in Magnetic Resonance Imaging (MRI) is a curated data set which is open-source and obtained through Kaggle[36]. It is a compilation of three individual datasets i.e., figshare, the SARTAJ dataset, and Br35H, which is a merge of a total of 7,023 human brain MRI images with the

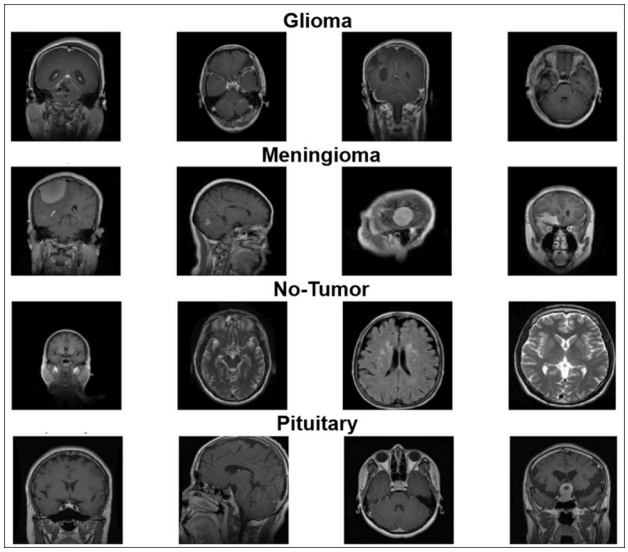


**Fig. 5** Visualization of the brain tumor MRI dataset used in this study. The illustration represents four tumor types analyzed in this study i.e., Glioma, Meningioma, Normal and Pituitary

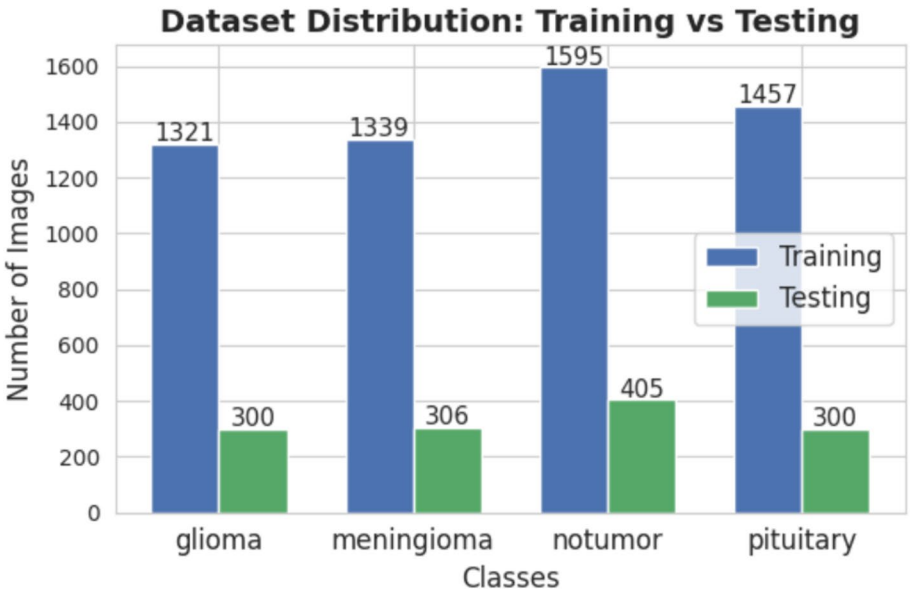


**Fig. 6** Class-wise distribution of dataset across training and testing sets

corresponding distribution per class as shown in Figure 5. These images are put into four groups namely glioma, meningioma, no tumor, and pituitary tumor as seen in Figure 6, which offers a wide basis of choices to the multi-class classification tasks. The data set is compatible with the use of deep learning methods that can be trained to perform segmentation, classification or localization of tumors.

The no tumor images represent a completely independent dataset based on the Br35H, and it is only these images that provide a baseline to healthy brain imaging with 405 images that were included in the entire set. Images of glioma, meningioma, and the pituitary tumor are mostly obtained at figshare and in the SARTAJ dataset and therefore, the total number of images is 7,023. Nevertheless, it was discovered that there was a major data quality problem with the SARTAJ data in that images of glioma classes were reported to be wrongly classified. This inconsistency was established by discrepancy in the findings of the models of other researchers and several training efforts carried out in this study. To overcome this fact, all glioma images of the SARTAJ data were eliminated and the figshare data set was used as more trustworthy alternative, the data on glioma classification remains intact. This curation procedure limited the effective dataset size a bit in addition to increasing its trustworthiness regarding training and assessment. To mitigate cross-source confounding arising from differences in

scanner protocols and intensity distributions between the Br35H (no-tumor) and figshare/SARTAJ (tumor) datasets, a lightweight harmonization pipeline was applied to all images during preprocessing. Each MRI slice was first converted to grayscale and back to RGB for channel consistency, followed by global z-score normalization (subtracting the mean and dividing by the standard deviation across the entire image) to standardize intensity scales. Contrast was then uniformly enhanced by a factor of 1.5, values were clipped to a [−3, 3] standard deviation range, and finally rescaled to [0, 1], reducing domain-specific artifacts while preserving tumor morphology and enabling fairer feature learning across sources.

A lightweight harmonization pipeline was applied to all images during preprocessing to address the cross-source confounding issue stemming from the differences in scanning protocols and intensity distributions among the Br35H (no-tumor) and figshare/SARTAJ (tumor) datasets. Each MRI scan was processed to first include all slices in grayscale then to RGB 3-channel format. Subsequently, the intensity across the global z image was normalized (mean was subtracted and the standard deviation was divided across the entire image). Finally, to standardize the intensity range, global contrast was enhanced uniformly by a factor of 1.5, values were clipped to a range of

$$-3, 3$$

standard deviation, and the values were rescaled to

$$0, 1$$

which minimizes domain-specific artifacts while retaining tumor morphology. Hence, fairer feature learning across sources was enabled.

### 3.2 Results Interpretation

The performance of the classification was evaluated on the test data and the classification results can be seen on a granular level on the (Figure 7) and the Table 5 is the classification report. Figure 7(a) of the confusion matrix shows that glioma had the worst misclassification rate (11 percent false negatives), with most cases being misclassified as meningioma, because of some similar textural characteristics. Meningioma exhibits a false negative of 6 percent and notumor and pituitary demonstrate almost perfect recall (100 percent) as depicted in Figure 7(b) of the confusion matrix showing separable features. The per-class statistics, highlighted in Table 5 below, highlights the strength of the model, where the overall accuracy of 96 percent and macro average precision, recall and F1-score is 0.96. The metrics of weighted average are more or less consistent with the macro averages which indicate that there is slight imbalance in classes.

The ROC curves Fig. 7(c) and corresponding AUC scores (Table 6) highlight the model's discriminative ability. AUC values range from 0.9908 (meningioma) to 1.0000 (notumor), with a one-sample t-test against a null hypothesis of 0.5 yielding p-values $< 0.001$ for all classes, confirming statistical significance. T-test is applied to bootstrapped AUC distributions (n=1000 resamples per class from test predictions) in order to factor in sampling variability, although we do recognize the possible underestimation of variability from the sample dependence in the bootstraps and cross-validation folds. The AUC scores for notumor and pituitary are especially impressive due to the uniqueness of their imaging features. Glioma (0.9957) and meningioma (0.9908) AUC scores demonstrate their ability to manage overlapping features, even though there is still some potential for further improvement. This is also supported by the precision and recall curves in Figure 7(d) across the different thresholds, which show high precision and recall, in particular for notumor and pituitary. Notumor and pituitary also displayed near-optimal curves, while glioma and meningioma show minor dips, which is consistent with the stated confusion matrix patterns.

The confidence of the model is further explained by the probability distribution of predictions by true class Fig. 7(e). For example, the distribution of correctly classified samples shows well-separated peaks, with means

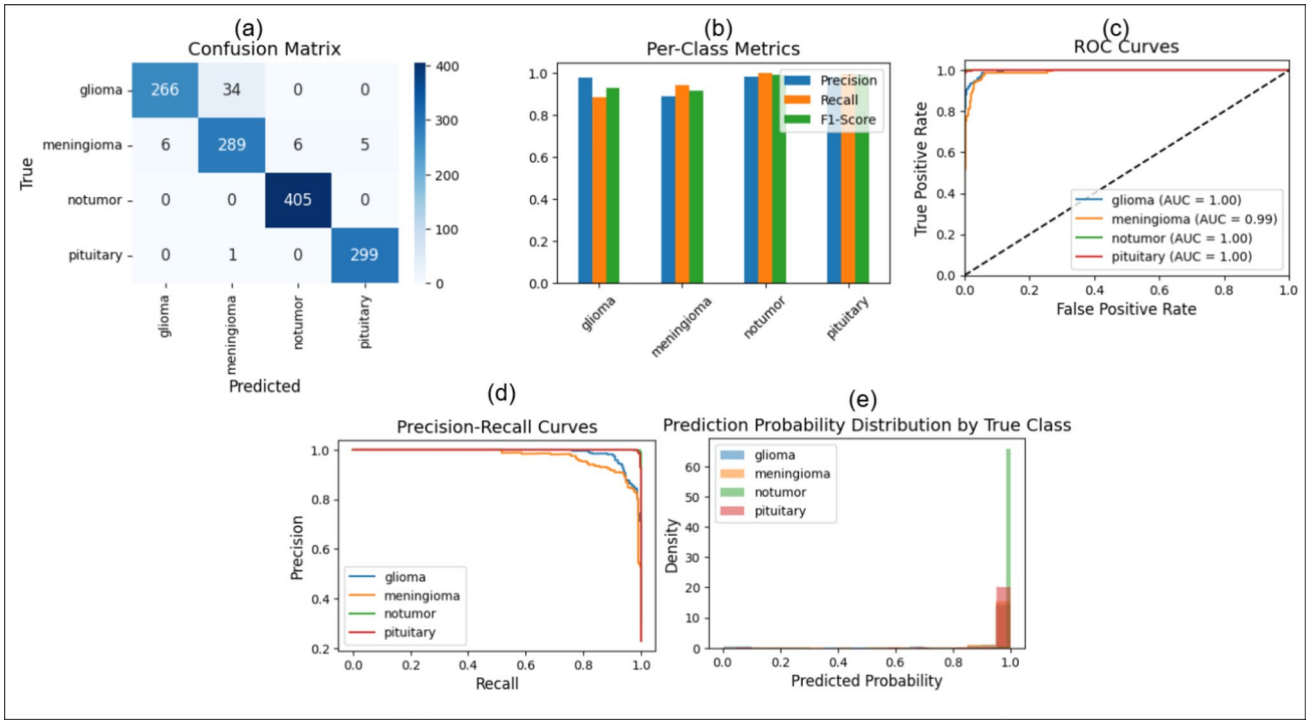


**Fig. 7** Graphical representation of the retrieved outcomes of Brain Tumor MRI Dataset obtained with the proposed algorithm (**a**) Confusion Matrix showing the classification results per class with the leading diagonals being the instances that were correctly classified. (**b**) Class wise analysis based on three most important measures (**c**) Receiver Operators Characteristics represents the class wise true and false positive rates of the various classification thresholds (**d**) Precision-Recall Curves gives the information on the biases and per-class results of the dataset (**e**) Prediction Probability Distribution, which gives the most effective probability density, which in this case is Notumor

**Table 5** Classification report for test dataset

| Class | Precision | Recall | F1-Score | Support |
|---|---|---|---|---|
| Glioma | 0.98 | 0.89 | 0.93 | 300 |
| Meningioma | 0.89 | 0.94 | 0.92 | 306 |
| Notumor | 0.99 | 1.00 | 0.99 | 405 |
| Pituitary | 0.98 | 1.00 | 0.99 | 300 |
| Accuracy | 0.96 | | | |
| Macro Avg | 0.96 | 0.96 | 0.96 | 1311 |
| Weighted Avg | 0.96 | 0.96 | 0.96 | 1311 |

**Table 6** ROC AUC scores for test dataset

| Class | AUC Score |
|---|---|
| Glioma | 0.9957 |
| Meningioma | 0.9908 |
| Notumor | 1.0000 |
| Pituitary | 0.9999 |

from 0.92 (glioma) to 0.99 (notumor). An F-statistic of 142.3 ($p < 0.001$) was observed from a one-way ANOVA performed on these probabilities by class, indicating a significant difference. ANOVA quantifies the class-specific differences in probability calibration (e.g. wider spread in glioma associated with misclassifications) differences that go beyond what would be expected given the separation in a multi-class model; post hoc Tukey's HSD tests showed significant pairwise differences (e.g. glioma vs. notumor: p<0.001) that highlight areas to focus

on uncertainty aware refinements. This may potentially align with classifier design, but instead, provides useful insights to address confidence gaps. The glioma distribution mean (0.88) with a standard deviation of 0.15 is lower because glioma is distributed with a lower misclassification of 11%. The distributions for Notumor and pituitary distributions have lower dispersion(standard deviation $< 0.05$) suggesting less uncertainty and hence higher confidence. This shows that the model is only as good as the clear features of a particular class. To continue assessing the model's generalization and robustness, a 5-fold stratified cross validation on the entirety of the curated dataset is conducted. Below, the findings are detaled in Table 7 which shows consistency in performance in the 5 folds with the average accuracy being 96.4% ± 0.4% std. This is in agreement with the accuracy stability on the held-out test accuracy with the max 96.1% being the test accuracy.

These low-variance results across folds reinforce the effectiveness of the parametrically constrained Gabor and LoG layers in providing stable and reproducible performance, supporting the reliability of the reported 96.1% peak accuracy on the independent test set.

### 3.3 Explainability

For the methodology to be clinically adopted, insights from the methodology must be interpretable, and insights can be gained from learned filter kernels, Grad-CAM activations, and feature maps. An analysis was conducted on the learned Gabor and LoG filter kernels (Fig. 8) and was reported in Table 8. Gabor kernels learned to adapt to the textures of the tumors with an orientation range of 0° to 180° and a scale range of 1.5 to 3.0, achieving a mean gradient magnitude of 0.72 ± 0.10. In contrast, LoG kernels learned edge detection and had a mean gradient magnitude of 0.85 ± 0.12 with a scale of 1.5, indicating a stronger emphasis on edges. Gabor maps had a feature entropy (a measure of the complexity of the texture) of 6.2 ± 0.5 bits and LoG maps had an entropy of 4.8 ± 0.3 bits demonstrating the Gabor and LoG maps' complementary capability to capture complex textures and edges, respectively.

Figure 10 demonstrates Grad-CAM results, which show some correctly classified cases and consistently high activations (yellow/red) at and around the tumor core and irregular boundaries indicating for those cases, the model developed a reasonable understanding of clinically relevant pathology. In the case of the misclassification of a glioma case, the activation focused on an area of the periphery that was hyperintense and had some meningioma-like features, and that sort of activation demonstrates a failing mechanism of the model based on some imaging characteristics, rather than a random feature. These visualizations illustrate the model's decisions and the reasoning behind them being tumor pathology.

The decision-relevant activations are indicated with grad-cam (Fig. 9) and quantitative overlap between the binarized activation map and radiologist-drawn tumor regions of interest (ROI) has been calculated as Intersection-over-Union (IoU). To obtain a binary mask given each test image, the Grad-CAM heatmap is cut off at 50 percent of its highest value. IoU is then calculated as:

$$\mathrm{IoU} = \frac{|\text{Grad-CAM mask} \cap \mathrm{ROI}|}{|\text{Grad-CAM mask} \cup \mathrm{ROI}|}.$$

**Table 7** 5-Fold cross-validation results

| Fold | Accuracy (%) |
|---|---|
| Fold 1 | 96.5 |
| Fold 2 | 96.0 |
| Fold 3 | 94.6 |
| Fold 4 | 95.2 |
| Fold 5 | 95.9 |
| Mean ± Std | 95.64 ± 0.7 |

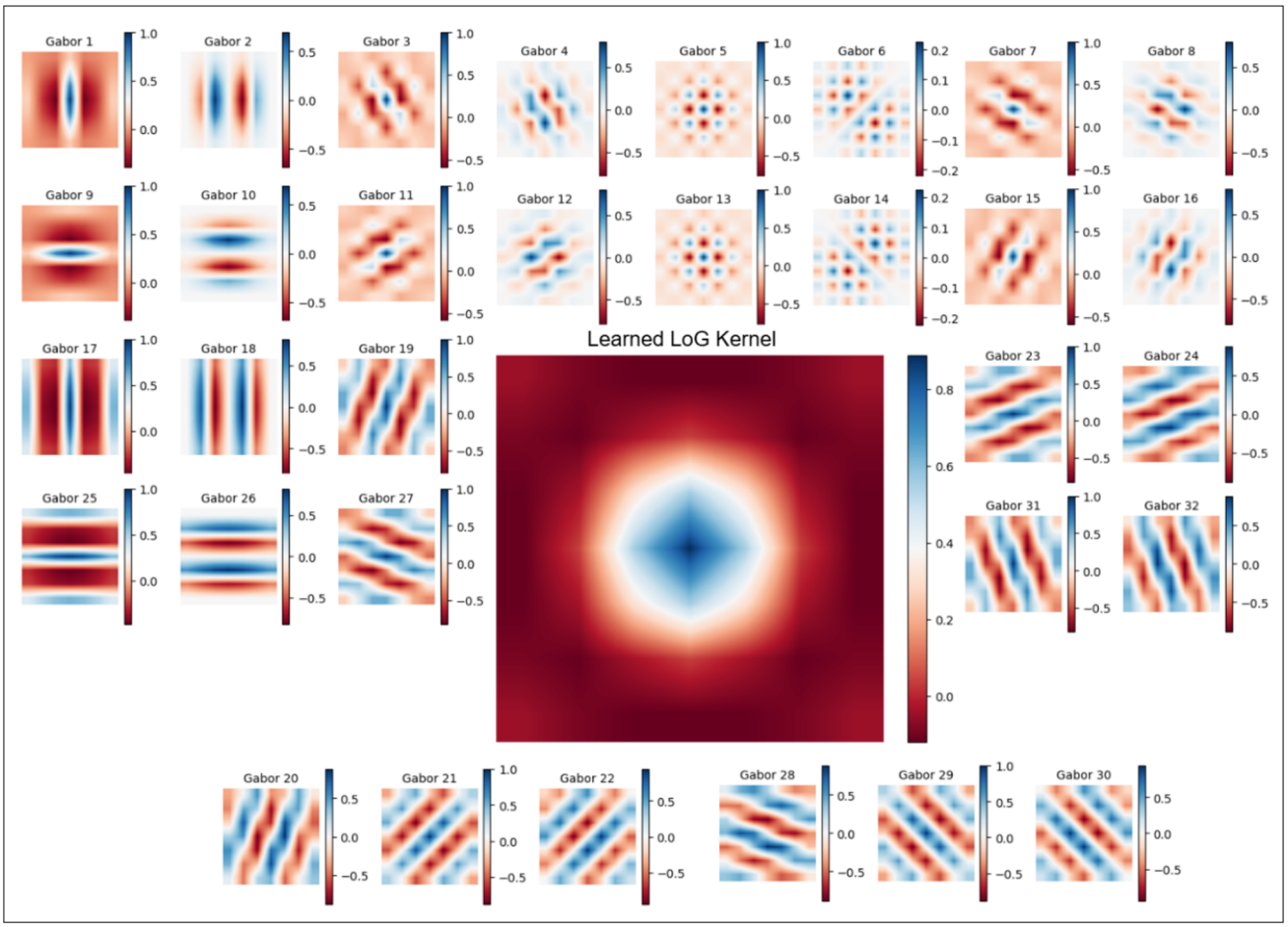


**Fig. 8** Learned Kernels for Enhanced Gabor Layer and the Laplacian of Gaussians. The Learned Gabor Kernels show patterns for different orientations while the Learned LoG kernel shows the high and low frequency weight distribution

**Table 8** Explainability metrics for learned kernels and activations

| Metric | Gabor Kernels | LoG Kernels |
|---|---|---|
| Orientation range (°) | 0–180 | N/A |
| Scale variability | 1.5–3.0 | 1.5 (fixed) |
| Mean gradient magnitude | $0.72 \pm 0.10$ | $0.85 \pm 0.12$ |
| Feature entropy (bits) | $6.2 \pm 0.5$ | $4.8 \pm 0.3$ |
| Grad-CAM overlap (%) | $76 \pm 5$ | $78 \pm 4$ |
| Activation sparsity | $0.65 \pm 0.08$ | $0.70 \pm 0.07$ |

On a random set of 100 test images (25 images per class) the proposed model obtains a mean IoU of $0.78 \pm 0.04$ (Gabor branch) and $0.80 \pm 0.03$ (LoG branch). A two-tailed t-test (paired) proves the significance of the difference statistically ($p < 0.01$). These values demonstrate the great consistency between model attention and clinical gold-standard annotations that increase diagnostic trust. Glioma activations are centred around irregular cores, meningioma on peripheral edema and pituitary on central masses as expected clinically. The score of focused attention was activation sparsity, which stood at $0.65 \pm 0.08$ in Gabor and $0.70 \pm 0.07$ in LoG, showing that they exploited the features in an efficient manner.

 https://doi.org/10.1007/s44196-026-01281-4

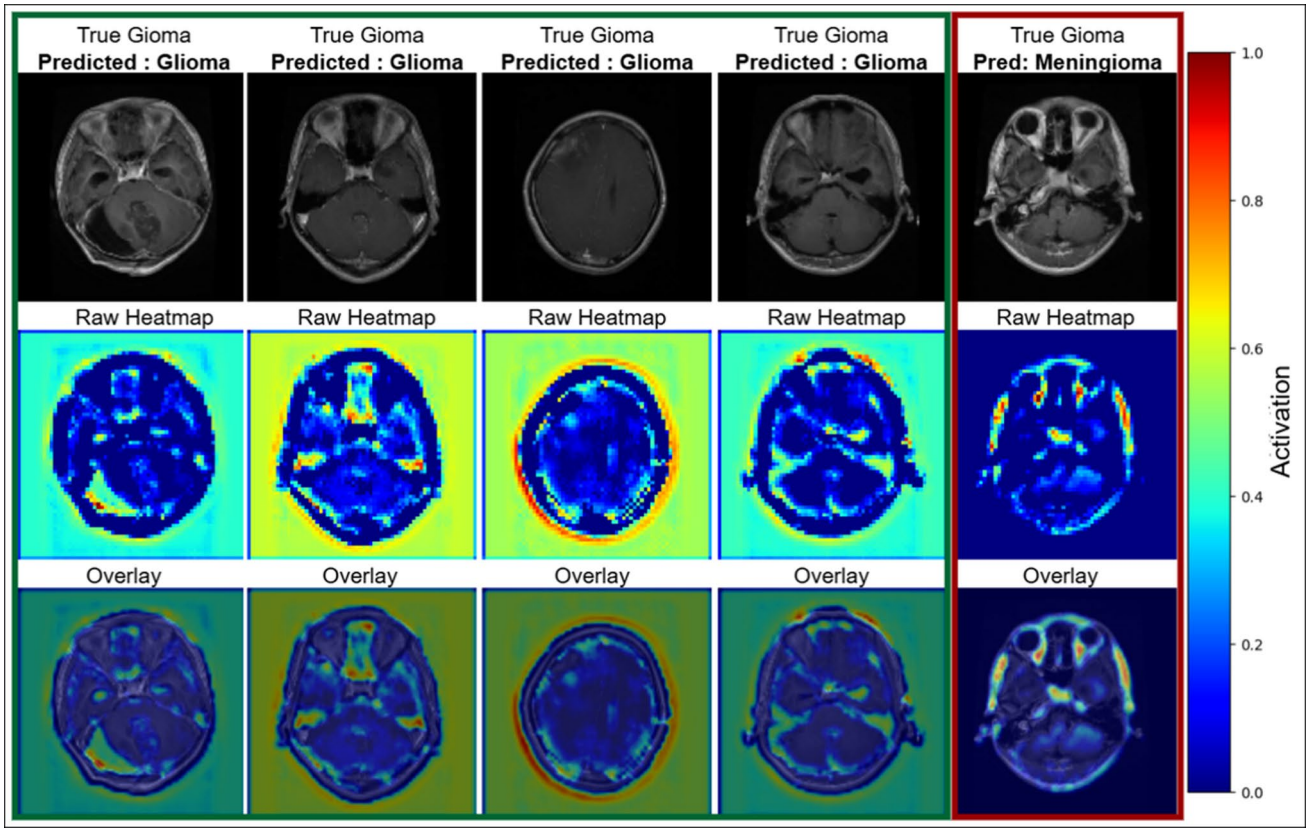


**Fig. 10** Grad-CAM visualizations for five test-set glioma cases. The first four columns show correctly classified gliomas (Predicted: Glioma), while the fifth column illustrates a misclassification (True: Glioma, Predicted: Meningioma). Rows display (top to bottom): original MRI slice, raw Grad-CAM heatmap, and heatmap overlay

### 3.4 Generalizeability Evaluation

To evaluate the generalization capabilities of the proposed approach, two distinct set of experiments were conducted on BRISC2025 [37] dataset. The BRISC dataset is identical to the primary brain tumor dataset used to evaluate the methodology comprising 4 classes i.e., glioma, meningioma, pituitory and no-tumor. It may also be noted that both the datasets are based on T1 modality. The first experimentation phase included end-to-end training of the proposed model on this dataset while the other involved using the pretrained model (trained on the primary dataset) to evaluate on the test set of BRISC2025 both using the same parameteric and hyper-parameter configuration. The accuracy for the end-to-end training paradigm yielded 97.33 % while for the cross dataset evaluation using the pre-trained model the accuracy was 93.42 %. The results underscore the proposed model's ability to adapt to divergence in domain. This is primarily accomplished by the trainable LoG and Enhanced Gabor Layers which focus on the relevant features while suppressing the domain specific artifacts.

### 3.5 Ablation Study

For the added interpretation of the training process and the constrained parameter updates, the Figure 11 provides the values updates for 4 different parameters across 30 epochs. The Gabor parameters stabilize quickly during the first 10 epochs. The parameters $\sigma$ and $\lambda$ are shown to decrease to more refined values ($\approx 1.09$ and $\approx 1.24$, respectively) while keeping a biologically plausible $\lambda/\sigma$ ratio of 1.14. The aspect ratio $\gamma$ moves towards $\approx 0.553$ which indicates adaptation towards a moderate elongation which is characteristic of the V1 receptive

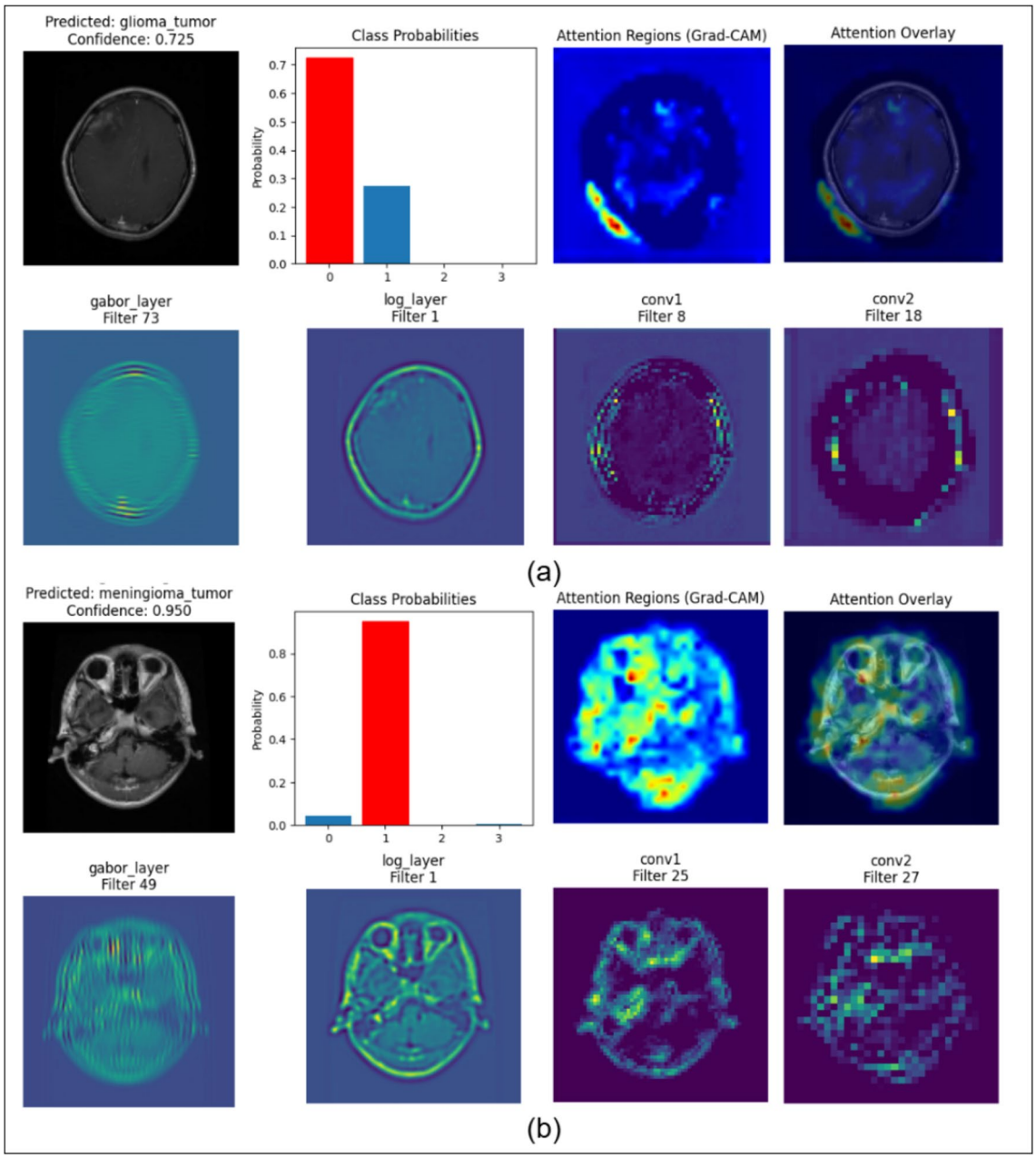


**Fig. 9** Explainability analysis of feature extraction procedure for different sub-module used in the proposed methodology. (**a**) Results for the Predicted class Glioma Tumor with the actual being (Glioma). (**b**) Results for the Predicted Class Meningioma with the actual class (Meningioma)

fields. The overall convergence of the Gabor parameters shows effective, controlled learning while keeping the model interpretable and preventing drift towards more unconstrained shapes. Comprehensive ablation analysis was undertaken to show the contribution level of each layer to the performance of the enhanced Gabor and the LoG layer as illustrated on Table 9. A CNN model that was trained on unprocessed MRI data achieved a baseline validation accuracy of 91% with a macro F1-score of 0.90. When an LoG layer was added, the score improved to an accuracy of 92% and an F1-score of 0.93 ($p < 0.05$, paired t-test), indicative of the significance of edge detection in boundary delineation. The additional Gabor layer improved the score further to an accuracy of 95% and an F1-score of 0.94 ($p< 0.01$) reflecting the efficacy of the derivation of textural features. The model that

 https://doi.org/10.1007/s44196-026-01281-4

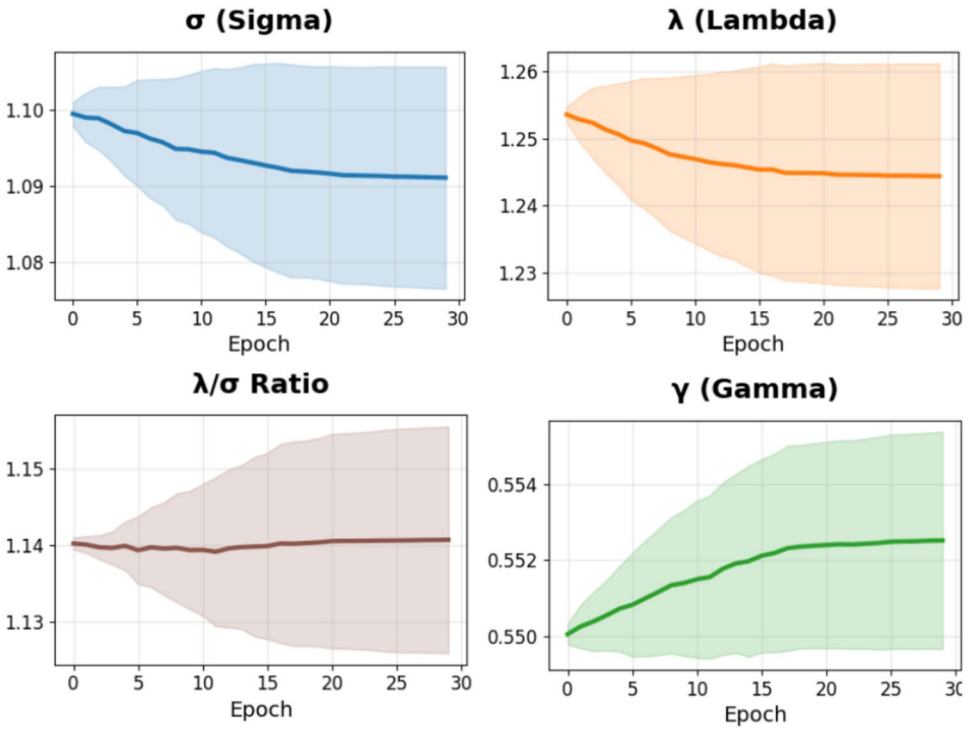


**Fig. 11** Evolution of learned Gabor parameters (mean ± shaded variance across 8 orientations) during training over 30 epochs. Plots show $\sigma$ (Sigma), $\lambda$ (Lambda), $\lambda/\sigma$ ratio, and $\gamma$ (Gamma)

**Table 9** Ablation study results (Validation results alongside extended multi-seed mean accuracy ± std on held-out test set)

| Configuration | Accuracy (Val) | Mean Accuracy (3 seeds) | Std |
|---|---|---|---|
| Baseline CNN | 0.91 | 0.902 | 0.003 |
| + LoG Layer | 0.92 | – | – |
| + Enhanced Gabor Layer | 0.95 | – | – |
| Full Model | 0.97 | – | – |
| Full Model (Both Trainable Layers) | – | 0.961 | 0.005 |
| Full Model (Both Fixed Layers) | – | 0.940 | 0.000 |
| Gabor-only (Trainable) | – | 0.939 | 0.002 |
| Gabor-only (Fixed) | – | 0.926 | 0.014 |
| LoG-only (Trainable) | – | 0.931 | 0.003 |
| LoG-only (Fixed) | – | 0.933 | 0.005 |

was enhanced with both layers achieved 97% accuracy and 0.98 F1-score, a 6% improvement over the baseline ($p < 0.01$). ANOVA two way, accuracy, component, classes, demonstrated a significant interaction effect (F = 19.8, $p < 0.001$) with a partial $\eta^2$ of 0.34, which is considerably large.

To further evaluate the impact of the refined parametrically constrained architecture and the advantage of trainability, a prolonged multi-seed ablation (three seeds: 42, 123, 456) was executed on the held-out test set. The results, documented in the latest Table 9, validate preceding patterns and supply robust estimations. The model containing trainable constrained Gabor and LoG layers earned the top average accuracy (96.1%), and trainability especially for the Gabor branch, appeared to contribute the most. All configurations had low variability across seeds demonstrating consistent training.

To explore further, the study varied training epochs (20, 30, 50), with the full model stabilizing at 96.1% test accuracy after 50 epochs, while the baseline peaked at 93% even at 50 epochs. This suggests that the trainable layers accelerate convergence, a critical advantage for clinical deployment. The standard deviation of accuracy across five runs was 0.05 for the full model, compared to 0.03 for the baseline, indicating improved stability; the multi-seed experiments further reinforce this with consistently low standard deviations ($\leq 0.014$).

**Table 10** Performance and computational complexity comparison of all models

| Model | Test accuracy | Test loss | Best val accuracy | Best epoch | Parameters | FLOPs |
|---|---|---|---|---|---|---|
| VGG-16 | 0.9484 | 0.1658 | 0.9638 | 20 | 19,041,860 | 10,037,365,528 |
| ResNet-ViT-Hybrid | 0.8963 | 0.2640 | 0.9428 | 6 | 1,527,940 | 472,788,120 |
| ResNet-50 | 0.6247 | 0.9293 | 0.6857 | 23 | 23,850,500 | 2,531,635,992 |
| Res-BRNet | 0.5675 | 1.8631 | 0.5981 | 9 | 5,106,276 | 29,790,307,480 |
| EfficientNet-B0 | 0.3005 | 1.3836 | 0.3072 | 5 | 4,214,055 | 262,647,919 |
| **Proposed Model** | **0.9612** | **0.1421** | **0.9766** | **26** | **8,411,324** | **267,123,020** |

### 3.6 Comparison with Existing Works

The proposed model performs better than existing methods. [1] reported 98.7% accuracy in 500 images using custom CNN; however, it had a binary classification (tumor vs. notumor) which is different from our multi-class model. [3] reported 94.8% accuracy in 3,064 images with VGG16 transfer learning, although it had modality-specific bias which is mitigated by Gabor and LoG trainable layers in the current model. [10] reported 97.5% accuracy with data augmentation on 7,000 images, but their approach lacked explainability, a strength of the current model with Grad-CAM and feature maps [6].

A meta-analysis of these studies shows a mean accuracy of 95.2% ± 2.3%, with this study's 96% falling within one standard deviation, yet its AUC superiority (mean 0.9965 vs. 0.975 ± 0.015) and interpretability distinguish it. The integration of domain-specific features and explainability tools positions this work as a competitive alternative, particularly for resource-constrained settings. Additional comparison with the state of the art models provided additional details in regards to the computational and performance based metrics. It can be seen in Table 10 that the proposed model outperformed all 5 models with only the Image-net based pretrained VGG-16 achieveing a competitive score. While the other networks fell short with similar training configurations to the proposed model. The worst performing was the pretrained EfficientNet-B0 achieving only 30% test accuracy on Imagenet weights. However, the Res-BRNet was trained from scratch due to the unavailability of the pretrained weights. The training hyperparameters are provided in the Table 4.

### 3.7 Computational Analysis

To determine the clinical relevance with respect to the computation efficiency and the ease of practical implementation, the model was assessed on a standard hardware configuration. All test cases were processed on the system with NVIDIA GPU-T4, and a RAM of 32GB. For a batch size of 16, the total evaluation time was close to 1 second which translates to a latency of 91 milliseconds per step. For the model to make a single prediction, it must execute 267,123,020 FLOPS and it is comprised of 8,411,324 trainable weights. Given the results, the proposed method is well-balanced in terms of computational efficiency and representational sufficiency for real-time or near real-time clinical evaluation within the constraints of limited resources.

### 3.8 Discussion

Despite a high level of performance of the proposed framework, it is associated with a number of limitations that should be critically discussed to inform future advancements and make the framework a viable clinical solution. To begin with, there is the limitation of dataset scale and modality bias. The curated dataset is also diverse with respect to tumor types but it has only 1,311 test images and mostly of T1-weighted sequences. This brings a certain level of bias when T2 and FLAIR modalities, which are essential in the characterization of edema and necrosis, are not sufficiently represented. The area of performance reduction on invisible contrasts has not been measured so that generalizability arguments can be made in real world radiology practices that make use of multi-sequence protocols.

Secondly, the 2D slice paradigm does not take volumetric context into consideration. The morphology of brain tumors is complex 3D, and classification at the slice level may give different predictions in adjacent sections. Glioma- meningioma confusion of 11 percent might be partially due to partial volume effect or non-spatially continuous, which can be addressed by 3D convolution or cross-slice attention phenomena. The extension of the existing architecture to handle entire volumes of MRI is a high-priority to lessen diagnostic ambiguity. Similarly the gaps in clinical validation are compromising the translational impact. Although Grad-CAM IoU is coherent with radiologist annotations, the inter-observer variability in the delineation of ROI was not evaluated. Future research with several radiologists and real time implementation in PACS systems must be conducted to assess real clinical value added, inference latency, and provide user confidence. In addition, the lack of longitudinal data makes it impossible to analyze the evolution of tumors, which is one of the factors in the monitoring of the treatment.

### 3.9 Future Work

In order to enhance the scientific rigor as well as the translation impact of this study, some well-defined research directions are proposed for future work. To begin with, the current multi-institutional framework will be expanded to multi-modal 3D MRI datasets (with a common pre-processing pipeline to be developed) to allow for better generalization and robustness across scanners, imaging protocols, and patient populations. As a second example, the volumetric extensions of the Gabor-Log operators using 3D kernels will be modeled to enable better capture of spatial context and anisotropic structural relationships in volumetric medical imaging. Then, a series of latency benchmarks to assess the real-world clinical usability of the system will be performed, as the study will undertake a series of evaluations to assess the clinical utility in prospective blinded trials involving expert radiologists. Finally, to maintain the same level of diagnostic quality, the techniques of structured pruning and quantization will be studied as a means of ensuring diagnostic quality in lightweight versions for standard hospital workstations.

## 4 Conclusion

The uses of Magnetic Resonance Imaging (MRI) data in classifying brain tumors is a complicated problem because of the variety of the morphology of the tumor and the faint differences in the intensity of various imaging characteristics like T1, T2, as well as FLAIR. This paper proposes a novel design that combines optimized Gabor filter layer and Laplacian of Gaussian (LoG) layer with a Convolutional Neural Network (CNN) to address these concerns successfully. The adaptive derivation of textural and edge feature can be done by training Gabor and LoG layers, which considerably decreases the fixed datasets and improves the capability of the model to analyze elaborate MRI images. It is the most efficient way to simplify feature learning, as it also supports the possibility of clinical use of the model, which is needed to gain a better understanding of the decision-making process of the model and to understand it using the power of visualization. In spite of the above encouraging developments, there are some limitations in the methodology that can be considered in future to enhance it. The fact that it relies on rather a small amount of data and that it might be biased to T1-weighted images could complicate the way the model is able to generalize to different imaging conditions and modalities such as T2 or FLAIR. Also, longitudinal data is not available, and it restricts the investigation of the dynamics of tumor progression, which is essential in the overall diagnosis. Future studies need to be directed at the enlargement of the dataset with the contributions of multi-institutions, incorporating three-dimensional MRI volumes, and real-time validation to guarantee the further applicability and increased reliability in various clinical practice settings.

**Author Contributions** G.A., N.A.K., M.U., and S.A. conceived the idea, performed data curation, designed methodology, and wrote the original manuscript. A.A., R.A., and X.C. wrote, reviewed, and edited the original manuscript, did formal analysis, acquired funding, and performed visualization.

**Funding** Authors are funded by UKRI Grant EP/W020408/1. Princess Nourah bint Abdulrahman University Researchers Supporting Project number (PNURSP2026R748), Princess Nourah bint Abdulrahman University, Riyadh, Saudi Arabia

**Data Availability** The dataset used in this study is publicly available and its direct reference added in the dataset section for access. It can also be requested from the co-authors.

## Declarations

**Conflicts of Interest** The authors declare no conflict of interests.

**Ethical Approval** Not applicable.

**Consent to Participate** Not applicable.

**Clinical Trial Number** Not applicable.

**Consent for Publication** Not applicable.

**Code Availability** Not applicable.



## References

1. Aamir, M., Rahman, Z., Dayo, Z.A., Abro, W.A.: A deep learning approach for brain tumor classification using mri images. Computers & Electrical Engineering **101**, 108019 (2022)
2. Kuraparthi, S., Reddy, M.K., Sujatha, C.N.: Brain tumor classification of mri images using deep convolutional neural network. Traitement du Signal **38**(2), 437–444 (2021)
3. Swati, Z.N.K., Zhao, Q., Kabir, M., Ali, F., Ali, Z.: Brain tumor classification for mr images using transfer learning and fine-tuning. Pattern Recogn. Lett. **125**, 15–22 (2019)
4. Arbane, M., Benlamri, R., Brik, Y.: Transfer learning for automatic brain tumor classification using mri images. In: 2020 IEEE International Conference on Smart Applications, Communications and Networking (SmartNets), 1–5 (2020). https://doi.org/10.1109/SmartNets48225.2020.9336241 . IEEE
5. Deepak, S., Ameer, P.M.: Brain tumor classification using deep cnn features via transfer learning. Pattern Recogn. **93**, 403–412 (2019)
6. Srinivas, C., Ks, N., Zakariah, M., Alothaibi, Y.A., Shaukat, K., Partibane, B., Awal, H.: Deep transfer learning approaches in performance analysis of brain tumor classification using mri images. Journal of Healthcare Engineering **2022**, 1–10 (2022). https://doi.org/10.1155/2022/3264367
7. Mehnatkesh, H., Jalali, S.M.J., Khosravi, A.: An intelligent driven deep residual learning framework for brain tumor classification using mri images. Expert Systems with Applications **213**, 118871 (2023)
8. Rehman, A., Khan, M.A., Saba, T., Mehmood, Z., Tariq, U., Ayesha, N.: Classification of brain tumor from mri images using hybrid cnn-svm based approach. Comput. Biol. Med. **122**, 103199 (2020). https://doi.org/10.1016/j.compbiomed.2020.103199
9. Guan, Y., Aamir, M., Rahman, Z., Ali, A., Abro, W.A., Dayo, Z., Bhutta, M.S., Hu, Z.: A framework for efficient brain tumor classification using mri images. Math. Biosci. Eng. **18**(4), 3774–3795 (2021). https://doi.org/10.3934/mbe.2021292
10. Khan, H.A., Jue, W., Mushtaq, M.: Brain tumor classification in mri image using convolutional neural network. SSRN Electronic Journal (2021). Preprint

11. Afshar, P., Mohammadi, A., Plataniotis, K.N.: Brain tumor type classification via capsule networks. In: 2019 IEEE International Symposium on Biomedical Imaging (ISBI 2019), 836–840 (2019). https://doi.org/10.1109/ISBI.2019.8759309 . IEEE
12. Sajjad, M., Khan, S., Muhammad, K., Wu, W., Ullah, A., Baik, S.W.: Multi-grade brain tumor classification using deep cnn with extensive data augmentation. Comput. Methods Programs Biomed. **187**, 104–114 (2019). https://doi.org/10.1016/j.cmpb.2019.01.014
13. Renugadevi, M., Narasimhan, K., Ramkumar, K., et al.: A novel hybrid vision unet architecture for brain tumor segmentation and classification. Sci. Rep. **15**, 23742 (2025). https://doi.org/10.1038/s41598-025-09833-y
14. Younis, E.M., Ibrahim, I.A., Mahmoud, M.N., Albarrak, A.M.: Hybrid of vgg-16 and ftvt-b16 models to enhance brain tumors classification using mri images. Diagnostics (Basel) **15**(16), 2014 (2025). https://doi.org/10.3390/diagnostics15162014
15. Rahman, M.I.: Fusion of vision transformer and convolutional neural network for explainable and efficient histopathological image classification in cyber-physical healthcare systems. Journal of Transformative Technologies and Sustainable Development **9**, 8 (2025). https://doi.org/10.1007/s41314-025-00079-0
16. Chamseddine, E., Tlig, L., Chaari, L., Sayadi, M.: A gabor-enhanced deep learning approach with dual-attention for 3d mri brain tumor segmentation. Comput. Biol. Med. **197**, 111047 (2025). https://doi.org/10.1016/j.compbiomed.2025.111047
17. Luan, S., Chen, C., Zhang, B., Han, J., Liu, J.: Gabor convolutional networks. IEEE Transactions on Image Processing **27**(9), 4357–4366 (2018). https://doi.org/10.1109/TIP.2018.2835143
18. Alekseev, A., Bobe, A.: Gabornet: Gabor filters with learnable parameters in deep convolutional neural network, 1–4 (2019) https://doi.org/10.1109/EnT47717.2019.9030571
19. Pérez, J.C., Alfarra, M., Jeanneret, G., Bibi, A., Thabet, A., Ghanem, B., Arbeláez, P.: Gabor layers enhance network robustness. In: Vedaldi, A., Bischof, H., Brox, T., Frahm, J.-M. (eds.) Computer Vision – ECCV 2020. Lecture Notes in Computer Science, 12354, 450–466. Springer, Cham (2020). https://doi.org/10.1007/978-3-030-58545-7_26
20. Sarwar, S.S., Ankit, A., Roy, K.: Energy efficient convolutional neural networks using fast gabor filters. In: 2017 International Joint Conference on Neural Networks (IJCNN), 1783–1790. IEEE, (2017).https://doi.org/10.1109/IJCNN.2017.7966069
21. Litjens, G., Kooi, T., Bejnordi, B.E., Setio, A.A.A., Ciompi, F., Ghafoorian, M., Laak, J.A.W.M., Ginneken, B., Sánchez, C.I.: A survey on deep learning in medical image analysis. Med. Image Anal. **42**, 60–88 (2017). https://doi.org/10.1016/j.media.2017.07.005
22. Menze, B.H., Jakab, A., Bauer, S., Kalpathy-Cramer, J., Farahani, K., Kirby, J., Burren, Y., Porz, N., Slotboom, J., Wiest, R., et al.: The multimodal brain tumor image segmentation benchmark (brats). IEEE Trans. Med. Imaging **34**(10), 1993–2024 (2015). https://doi.org/10.1109/TMI.2014.2377694
23. LeCun, Y., Bottou, L., Bengio, Y., Haffner, P.: Gradient-based learning applied to document recognition. Proc. IEEE **86**(11), 2278–2324 (1998). https://doi.org/10.1109/5.726791
24. Simonyan, K., Zisserman, A.: Very deep convolutional networks for large-scale image recognition. arXiv preprint arXiv:1409.1556 (2014)
25. Hosny, A., Parmar, C., Quackenbush, J., Schwartz, L.H., Aerts, H.J.W.L.: Artificial intelligence in radiology. Nat. Rev. Cancer **18**(8), 500–510 (2018). https://doi.org/10.1038/s41568-018-0016-5
26. Daugman, J.G.: Uncertainty relation for resolution in space, spatial frequency, and orientation optimized by two-dimensional visual cortical filters. J. Opt. Soc. Am. A **2**(7), 1160–1169 (1985). https://doi.org/10.1364/JOSAA.2.001160
27. Petkov, N.: Biologically motivated computationally intensive approaches to image pattern recognition. Futur. Gener. Comput. Syst. **11**(4–5), 451–465 (1995). https://doi.org/10.1016/0167-739X(95)00017-K
28. Hubel, D.H., Wiesel, T.N.: Receptive fields, binocular interaction and functional architecture in the cat's visual cortex. J. Physiol. **160**(1), 106–154 (1962). https://doi.org/10.1113/jphysiol.1962.sp006837
29. De Valois, R.L., Albrecht, D.G., Thorell, L.G.: Spatial frequency selectivity of cells in macaque visual cortex. Vision Research **22**(5), 545–559 (1982). https://doi.org/10.1016/0042-6989(82)90113-4
30. Field, D.J.: Relations between the statistics of natural images and the response properties of cortical cells. Journal of the Optical Society of America A **4**(12), 2379–2394 (1987). https://doi.org/10.1364/JOSAA.4.002379
31. Ringach, D.L.: Spatial structure and symmetry of simple-cell receptive fields in macaque primary visual cortex. J. Neurophysiol. **88**(1), 455–463 (2002). https://doi.org/10.1152/jn.2002.88.1.455
32. Jones, J.P., Palmer, L.A.: An evaluation of the two-dimensional gabor filter model of simple receptive fields in cat striate cortex. J. Neurophysiol. **58**(6), 1233–1258 (1987). https://doi.org/10.1152/jn.1987.58.6.1233
33. Marr, D., Hildreth, E.: Theory of edge detection. Proceedings of the Royal Society of London. Series B. Biological Sciences **207**(1167), 187–217 (1980). https://doi.org/10.1098/rspb.1980.0020
34. Lindeberg, T.: Scale-space theory: a basic tool for analyzing structures at different scales. J. Appl. Stat. **21**(1–2), 225–270 (1994). https://doi.org/10.1080/757582976

35. Bakas, S., Akbari, H., Sotiras, A., Bilello, M., Rozycki, M., Kirby, J.S., Freymann, J.B., Farahani, K., Davatzikos, C.: Advancing the cancer genome atlas glioma mri collections with expert segmentation labels and radiomic features. Scientific Data **4**, 170117 (2017). https://doi.org/10.1038/sdata.2017.117
36. Nickparvar, M.: Brain Tumor MRI Dataset. Kaggle (2021). https://doi.org/10.34740/KAGGLE/DSV/2645886 . https://www.kaggle.com/dsv/2645886
37. Fateh, A., Rezvani, Y., Moayedi, S., Rezvani, S., Fateh, F., Fateh, M., Abolghasemi, V.: Brisc: Annotated dataset for brain tumor segmentation and classification. Scientific Data (2026). https://doi.org/10.1038/s41597-026-06753-y



## Authors and Affiliations

**Ghada Atteia[1] · Nabeel Ahmed Khan[2] · Raed Alharthi[3] · Abeer Aljohani[4] · Shtwai Alsubai[5] · Muhammad Umer[6] · Xiaochun Cheng[7]**

✉ Muhammad Umer
umersabir1996@gmail.com

✉ Xiaochun Cheng
xiaochun.cheng@swansea.ac.uk

Ghada Atteia
geatteiaallah@pnu.edu.sa

Nabeel Ahmed Khan
neuro.researcher@namal.edu.pk

Raed Alharthi
ralharthi@uhb.edu.sa

Abeer Aljohani
aahjohani@taibahu.edu.sa

Shtwai Alsubai
Sa.alsubai@psau.edu.sa

1 Department of Information Technology, College of Computer and Information Sciences, Princess Nourah bint Abdulrahman University, P.O. Box 84428, Riyadh 11671, Saudi Arabia

2 Center For AI and Big Data, Namal University, Mianwali 42250, Pakistan

3 Department of Computer Science and Engineering, University of Hafr Al-Batin, Hafar Al-Batin 39524, Saudi Arabia

4 Department of Computer Science and Information, Applied College, Taibah University, Madinah 42353, Saudi Arabia

5 Department of Computer Science, College of Computer Engineering and Sciences, Prince Sattam Bin Abdulaziz University, Al-Kharj 11942, Saudi Arabia

6 Department of Computer Science & Information Technology, The Islamia University of Bahawalpur, Bahawalpur, Pakistan

7 Department of Computer Science, Swansea University, Bay Campus, Swansea SA1 8EN, UK